16th Australasian Fluid Mechanics Conference
Crown Plaza, Gold Coast, Australia
2-7 December 2007

# Simulation of $CO_2$–$N_2$ expansion tunnel flow for the study of radiating bluntbody shock layers

**D. F. Potter[1], R. J. Gollan[1], T. Eichmann[2], P. A. Jacobs[1], R. G. Morgan[1] and T. J. McIntyre[2]**

[1]Department of Mechanical Engineering
[2]Department of Physics
University of Queensland, St Lucia, QLD 4072, AUSTRALIA

## Abstract

A 25 MJ/kg $CO_2$–$N_2$ expansion tunnel condition has been developed for the X2 impulse facility at the University of Queensland. A hybrid Lagrangian and Navier–Stokes computational simulation technique is found to give good correlation with experimentally measured shock speeds and pressure traces. The use of an inertial diaphragm model for describing secondary diaphragm rupture is found to estimate between 4% and 25% more $CO_2$ recombination over the test time than the widely accepted holding-time model. The obtained freestream conditions are assessed for application to proposed bluntbody spectroscopy and subscale aeroshell experiments. The chemically and vibrationally excited freestream test gas is found to prevent exact thermochemical similarity from being achieved, and the strong radiation–flowfield coupling characteristic of Mars aerocapture conditions cannot be reproduced experimentally.

## Introduction

RADIATIVE heating is an important consideration for the design of aeroshells to be used for proposed aerocapture missions. Atmospheric interface velocities for viable manned aerocapture missions to Mars have been estimated to be between 6.0 km/s and 8.6 km/s, with radiation contributing at least 80% of the incident heat flux at velocities over 8.5 km/s [1]. The accepted Martian atmospheric composition as determined by the Viking 1 lander is 95.7% $CO_2$, 2.7% $N_2$ and 1.6% Ar by volume. At aerocapture conditions $CO_2$ quickly dissociates behind the shock layer into CO and O, while substanital $N_2$ dissociation also occurs. Additional exchange reactions involving these species leads to the production of C, CO, $C_2$ and CN, all of which are known to be strong radiators [2]. In addition, low freestream densities and high velocities induce a state of thermochemical nonequilibrium in the aeroshell shock layer. Reducing the uncertainty of nonequilibrium radiation predictions has been identified as one of the highest priorities in planetary-entry gas dynamics today [3].

A series of experiments are being undertaken in the X2 impulse facility to provide a physical reference for the computational modelling of radiating shock layers. Two distinct modes of operation have been developed — (a) non-reflected shock tube operation, and (b) expansion tunnel operation. While the non-reflected shock tube mode can provide accurate replication of true flight stagnation streamline conditions, the expansion tunnel mode of operation allows for investigation of radiating shock layers formed over subscale aeroshell models and bluntbody test articles. A sting-mounted subscale aeroshell model in the X2 test section is illustrated in Figure 1. Approximate radiative similarity with the true flight conditions can be achieved by matching the binary scaling parameter, $\rho L$ [4]. This methodology has been employed for the experimental measurement of radiative and convective transfer rates to a Titan aerocapture model using thin-film gauges in the larger X3 facility at the University of Queensland [5].

The binary scaling rationale, however, breaks down for strongly radiating and nonequilibrium flowfields. This paper aims to assess the suitability of a 25 MJ/kg $CO_2$–$N_2$ expansion tunnel condition for bluntbody spectroscopy and subscale aeroshell experiments. Detailed CFD simulations of the complete X2 facility are performed and compared against experimentally obtained pressure measurements. This paper builds on previous work involving large-scale axisymmetric, finite-rate chemistry simulations of the X2 [6] and larger X3 facilities [7]. Specifically, extensions are made to model a reacting $CO_2$–$N_2$ mixture and investigate the extent of thermal nonequilibrium during the expansion of the test gas through the nozzle. The obtained freestream conditions are then used to investigate the use of subscale models for representing true flight conditions.

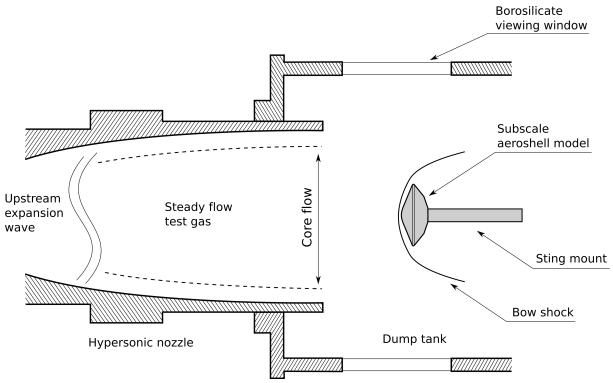


Figure 1: Schematic of a sting-mounted subscale aeroshell model in the X2 expansion tunnel test section.

## Experimental description

### The X2 impulse facility

A schematic and space-time diagram of the X2 impulse facility operated as an expansion tunnel is shown in Figure 2. The facility is driven by a 35 kg single-stage piston and currently operates with a compression ratio of 1:500 in the driver tube. The primary diaphragms are 1.2 mm cold rolled steel and are scored to ensure clean rupture at 15 MPa. The 85 mm bore shock and expansion tubes are 3.4 m and 5.2 m in length respectively. For the present work, a Mach 10 full capture hypersonic nozzle designed by Scott [8] was attached to the end of the acceleration tube. The hypersonic nozzle has an area ratio of 6 and typically gives a coreflow diameter in excess of 140 mm.

A total of 9 PCB pressure transducers are flush-mounted throughout the shock and expansion tubes, and allow the recording of static pressure histories and subsequent shock speed determination. An additional pair of static pressure transducers are installed at the exit plane of the nozzle. During the development of the conditions, a Pitot rake spanning 140 mm of the flow with 9 transducers was installed in the test section.

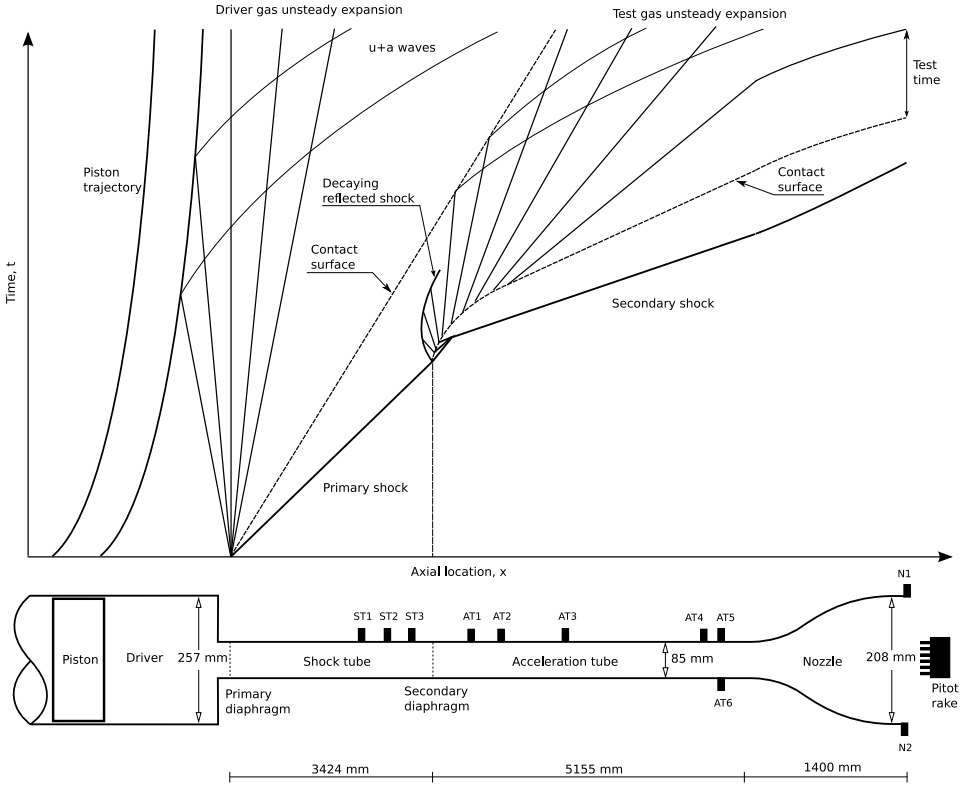


Figure 2: Schematic and space-time diagram of the X2 impulse facility operated as an expansion tunnel.

#### 25 MJ/kg $CO_2$–$N_2$ condition

A 25 MJ/kg $CO_2$–$N_2$ expansion tunnel condition with freestream density of 1.6 g/m$^3$ and velocity of 6.4 km/s has been developed for the X2 impulse facility. A summary of the initial fill conditions, experimentally measured shock speeds and computationally simulated freestream conditions are shown in Table 1. The simulated Mars test gas is conservatively taken to be 96% $CO_2$ – 4% $N_2$ by volume. Scored primary diaphragms have recently been implemented to minimise debris and damage to models and sensors in the test section. Further reduction of debris and carbon based contaminants was achieved through the use of 10 $\mu$m aluminium sheets in place of 13 $\mu$m Mylar at the secondary diaphragm location. A total of 109 shots targetting this condition have been conducted in the X2 facility over the past 12 months. A sample population of 23 shots with Pitot and static pressure measurements of the test flow are taken to be representative of the nominal condition — the experimental values shown in Table 1 are the means of this population. The calculated freestream conditions are obtained from a hybrid simulation technique to be described in the proceeding section.

#### A chemical kinetic model for $CO_2$–$N_2$ mixtures

The chemical kinetics of the $CO_2$–$N_2$ test gas needs to be described over a wide density and enthalpy range for the present work. Whilst mixtures of equilibrium and ideal gases are sufficient to describe the free-piston compression and high pressure shock tube, nonequilibrium processes are significant in the low pressure, high Mach number flow downstream of the secondary diaphragm. The test gas will be in a state of chemical nonequilibrium through the unsteady expansion following diaphragm rupture, whilst the thermal modes are anticipated to be in equilibrium. Conversely, frozen chemistry and thermal nonequilibrium are expected as the test gas expands steadily through the hypersonic nozzle and into the dump-tank. Finally, both thermal and chemical nonequilibrium will occur in the bluntbody shock layer. An extensive review of 10 thermochemical models for the Martian atmosphere was conducted in 2006 by Ndindabahizi et al [9]. The two-temperature model and extensive reaction scheme of Park et al [10] performed well and is widely accepted as a benchmark model due to its reliability and relative simplicity. This model has been implemented for the present work with an improved thermochemical coupling module.

#### Single-temperature formulation

A single-temperature $CO_2$–$N_2$ reaction scheme is required for the viscous Navier-Stokes simulation of the expansion tunnel. The extent of thermal nonequilibrium through the nozzle expansion will be investigated using a simplified, quasi-one-dimensional, space-marching analysis. The stagnated test gas upstream of the secondary diaphragm just prior to rupture contains negligible ionic species, and therefore all ionic reactions can be omitted for the expansion tunnel simulations. The neutral dissociation and exchange reactions considered by Park, with the exception of those involving the NCO molecule which is a minor species, are reactions 1 through 16 as listed in Table 2. The forward rates for all reactions are calculated through the generalised Arrhenius formulation with the rate constants provided by Park et al [10], and backward rates obtained from the respective equilibrium constants. The $CO_2$–$N_2$ test gas is treated as a mix of thermally perfect species. Viscosity and thermal conductivity are calculated using the curve fits and expressions for mixtures of thermally perfect gases used by NASA's Chemical Equilibrium with Applications (CEA) program [11].

#### Two-temperature formulation

The two-temperature model considers the subdivision of thermal energy into two distinct modes — translational and rotational energy in the 'transrotational' mode with temperature

| | |
|---|---|
| **Fill conditions** | |
| Reservoir | 1.28 MPa Air |
| Compression tube | 30 kPa 25% Ar – 75% He |
| Shock tube | 3.5 kPa 96% $CO_2$ – 4% $N_2$ |
| Acceleration tube | 8 Pa Air |
| **Diaphragms** | |
| Primary diaphragm | Scored 1.2 mm steel |
| Secondary diaphragm | 13 $\mu$m Mylar (or) 10 $\mu$m Al |
| **Measured Shock speeds** | |
| $U_{s,st}$ | $3240 \pm 50$ m/s |
| $U_{s,at}$ | $6340 \pm 230$ m/s |
| **Simulated Shock speeds** | |
| $U_{s,st}$ | $3300 \pm 50$ m/s |
| $U_{s,at}$ | $6310 \pm 220$ m/s |
| **Measured freestream conditions** | |
| $p_{static}$ | $500 \pm 170$ Pa |
| $p_{pitot}$ | $85 \pm 20$ kPa |
| Test time, $\tau$ | 150 $\mu s$ |
| **Simulated freestream conditions** | |
| Total enthalpy, $h_{total}$ | 24.7 MJ/kg |
| Effective flight velocity, $v_\infty$ | 7030 m/s |
| Velocity, $u$ | $6400 \pm 150$ m/s |
| Density, $\rho$ | $1.63 \pm 0.3$ g/m$^3$ |
| Temperature, $T$ | $860 \pm 100$ K |
| $CO_2$ mole fraction, $X_{CO_2}$ | $0.36 \pm 0.04$ |
| Mach number, M | $12.5 \pm 0.5$ |
| Unit Reynold's number, Re | $2.70 \times 10^5$ m$^{-1}$ |

Table 1: Fill conditions, shock speeds and freestream conditions for the 25 MJ/kg $CO_2$–$N_2$ X2 expansion tunnel condition.

| | Reactions | Energy of reaction |
|---|---|---|
| | *Dissociation reactions* | |
| 1 | $CO_2 + M \Longleftrightarrow CO + O + M$ | -526 kJ/mol |
| 2 | $CO + M \Longleftrightarrow C + O + M$ | -1073 kJ/mol |
| 3 | $N_2 + M \Longleftrightarrow N + N + M$ | -941 kJ/mol |
| 4 | $O_2 + M \Longleftrightarrow O + O + M$ | -497 kJ/mol |
| 5 | $NO + M \Longleftrightarrow N + O + M$ | -628 kJ/mol |
| 6 | $CN + M \Longleftrightarrow C + N + M$ | -590 kJ/mol |
| 7 | $C_2 + M \Longleftrightarrow C + C + M$ | -581 kJ/mol |
| | *Exchange reactions* | |
| 8 | $NO + O \Longleftrightarrow N + O_2$ | -162 kJ/mol |
| 9 | $N_2 + O \Longleftrightarrow N + O_2$ | -319 kJ/mol |
| 10 | $CO + O \Longleftrightarrow C + O_2$ | -575 kJ/mol |
| 11 | $CO + C \Longleftrightarrow C_2 + O$ | -48 kJ/mol |
| 12 | $CO + N \Longleftrightarrow CN + O$ | -321 kJ/mol |
| 13 | $N_2 + C \Longleftrightarrow CN + N$ | -193 kJ/mol |
| 14 | $CN + O \Longleftrightarrow NO + C$ | -121 kJ/mol |
| 15 | $CN + C \Longleftrightarrow C_2 + N$ | -11 kJ/mol |
| 16 | $CO_2 + O \Longleftrightarrow O_2 + CO$ | -231 kJ/mol |
| | *Associative ionisation reactions* | |
| 17 | $N + O \Longleftrightarrow NO^+ + e^-$ | -265 kJ/mol |
| 18 | $O + O \Longleftrightarrow O_2^+ + e^-$ | -670 kJ/mol |
| 19 | $C + O \Longleftrightarrow CO^+ + e^-$ | -275 kJ/mol |
| | *Charge exchange reactions* | |
| 20 | $NO^+ + C \Longleftrightarrow NO + C^+$ | -193 kJ/mol |
| 21 | $O_2^+ + O \Longleftrightarrow O^+ + O_2$ | -150 kJ/mol |
| 22 | $NO^+ + N \Longleftrightarrow O^+ + N$ | -106 kJ/mol |
| 23 | $NO^+ + O \Longleftrightarrow O_2^+ + N$ | -404 kJ/mol |
| 24 | $CO + C^+ \Longleftrightarrow CO^+ + C$ | -261 kJ/mol |
| 25 | $O_2 + C^+ \Longleftrightarrow O_2^+ + C$ | -78 kJ/mol |
| | *Electron-impact ionisation reactions* | |
| 26 | $C + e^- \Longleftrightarrow C^+ + e^- + e^-$ | -1087 kJ/mol |
| 27 | $O + e^- \Longleftrightarrow O^+ + e^- + e^-$ | -1318 kJ/mol |

Table 2: Neutral and ionic chemical reactions included in the $CO_2$ – $N_2$ reaction scheme [10].

$T_{tr}$, vibrational and electronic energy in the 'vibroelectronic' mode with temperature $T_{ve}$. All molecules are described vibrationally as truncated harmonic oscillators, and electronically by the ground and first excited states only. The collisional encounters of $N_2$, CO and $CO_2$ with N, O, C, $N_2$, CO and $CO_2$ are considered. The Landau-Teller model is implemented for describing vibrational relaxation towards the transrotational temperature for each of these encounters. The induction time $\tau$ is obtained through the Millikan and White [12] expression with the high-temperature correction for induction phenomena as devised by Park [2]. The coupled vibration-chemistry-vibration (CVCV) model of Knab et al [13] has previously been implemented in `libgas2` for application to diatomic molecules with unique vibrational temperatures. Modifications have been made to permit the use of this thermochemical coupling module for polyatomic $CO_2$ molecules in the present work.

#### X2 expansion tunnel simulations

The computational approach for expansion tunnel simulation implemented here considers four distinct stages — (1) free-piston compression and primary diaphragm rupture, (2) high pressure, low Mach number shock tube flow, (3) secondary diaphragm rupture, and (4) low pressure, high Mach number acceleration tube, hypersonic nozzle and dumptank expansion. The first three stages involve all the important flow processes occurring at reasonably high pressures ($p > 100$ kPa) and low Mach numbers ($M < 4$). The in-house quasi-one-dimensional Lagrangian code `L1d2` [14] performs well in this regime, and is therefore used for simulating the X2 expansion tunnel flow up to and including the secondary diaphragm rupture.

#### Free-piston compression and shock tube flow

The quasi-one-dimensional nature of the `L1d2`geometry can result in boundary layer heat loss being significantly underestimated. Previous attempts at modelling the free-piston compression of the driver gas have demonstrated this inadequacy, with the driver gas temperature at primary diaphragm rupture being unreasonably high. The `L1d2` simulation of the shock tube flow is therefore begun at the moment of primary diaphragm rupture. The driver gas pressure and slug-length at rupture are obtained from an idealised model of the free-piston compression, whilst the temperature is obtained parametrically by matching the experimentally measured primary shock speed. Momentum loss at the primary diaphragm station area change is accounted for through a loss-per-unit-length factor $K_L$ of 0.25. The $CO_2$–$N_2$ test gas is described by an equilibrium equation-of-state using the curve fits provided by the CEA program [11], as are the respective transport coefficients. The Ar–He driver gas is described as a viscous mixture of ideal gases.

#### Light secondary diaphragm rupture

When the primary shock through the stagnant test gas reaches the light secondary diaphragm, the first few millimeters of shock-processed test gas are stagnated by the resulting reflected shock. For the condition at hand the ratio of the stagnated to freestream density of the test gas is approximately $10^4 : 1$ — thus, taking area change into account and using the freestream conditions from Table 1, the observed 150 $\mu s$ of test flow originates from within the first 2 mm of stagnated test gas. It follows that the subsequent expansion of this very small test gas volume through the acceleration tube and nozzle must be modelled accurately.

Diaphragms are typically modelled in `L1d2` as fixed-wall

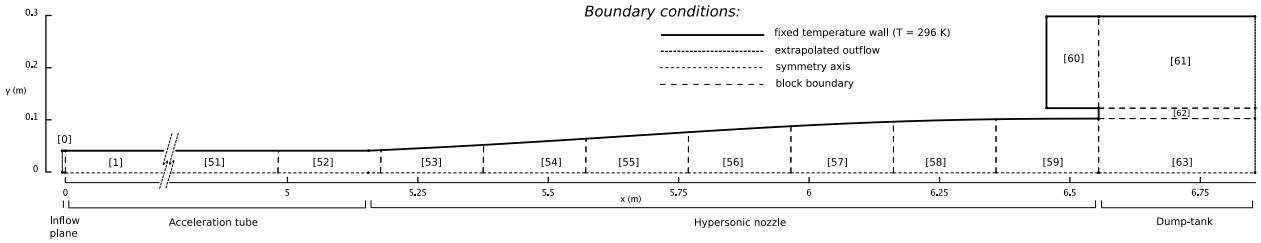


Figure 4: Computational domain for axisymmetric simulation of the X2 facility operated as an expansion tunnel

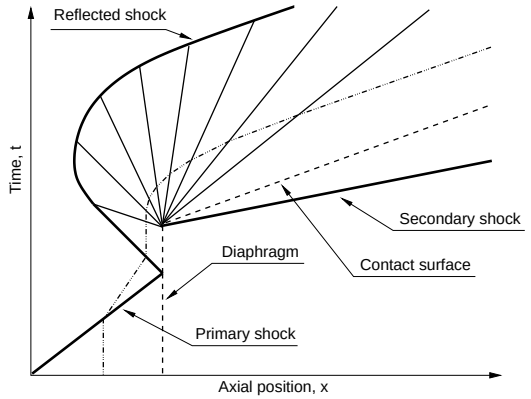


(a) Holding time model

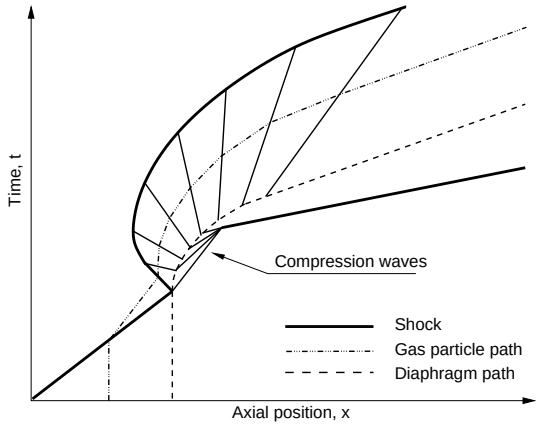


(b) Inertial diaphragm model

Figure 3: Space-time diagrams of light secondary diaphragm rupture in an expansion tube (adapted from Bakos and Morgan [15]).

boundary conditions that can be triggered by exceeding a user specified pressure difference between the two adjacent gas slugs. Once triggered, the fixed-wall boundary conditions stay in place for small period of time to allow the reflected shock to form, and then are removed to allow the adjacent gas slugs to interact. This method of modelling diaphragms is referred to as the holding-time model, and adequately captures the physical processes for most conditions. Bakos and Morgan [15] demonstrated the limitations of the holding-time model through comparision with an inertial diaphragm model. Space-time representations of both the holding-time and inertial diaphragm models are shown in Figure 3. The inertial diaphragm model represents the diaphragm as an ideal piston — the diaphragm shears cleanly at the tube wall, remains planar during its motion and provides only inertial resistance to the expanding test gas. Where a test gas particle immediately upstream of the secondary diaphragm experiences an infinite rate of expansion under the holding-time model, the inertial diaphragm model shows the contact surface must accelerate to an asymptotic limit over a finite period of time. The duration a test gas particle spends in the unsteady expansion directly determines the degree of thermochemical relaxation experienced — large expansion rates will result in frozen thermochemistry, while low expansion rates will tend towards equilibrium.

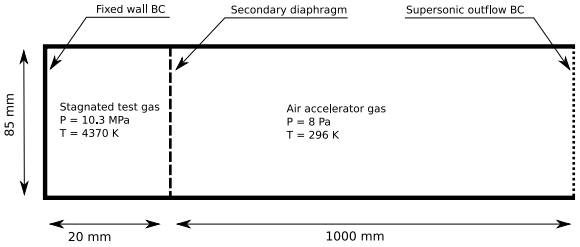


Figure 5: Computational geometry for nonequilibrium Lagrangian simulations of thermochemical relaxation through the unsteady expansion.

Simulations of the unsteady expansion are performed with the `L1d2` code modified to handle gases in thermochemical nonequilibrium. The high temperature correction for elastic collisions is omitted as it is not applicable in the relatively moderate temperature range encountered ($T < 5000$ K). A schematic of the `L1d2` geometry is shown in Figure 5. The reflected shock processed test gas is represented as a 20 mm slug at the stagnation conditions determined by the equilibrium `L1d2` simulations of the shock tube. The selection of such a large slug length was done on the assumption that the reflected shock will process the first 2 mm of eventual test gas before the tail of the expansion wave catches up. Therefore any pressure and entropy relief effect on the reservoir of stagnated test gas is not captured by this analysis.

#### Acceleration tube, nozzle and dumptank flow

Another in-house code, `mbcns2` (a Multi-Block Compressible Navier-Stokes solver) [16], is used for the low pressure, high Mach number acceleration tube, nozzle and dumptank flow. `mbcns2` integrates the cell-centred finite-volume formulation of the Navier-Stokes equations and has a shock-capturing ability through the use of a limited reconstruction scheme and an upwind-biased flux calculator. The computational domain is subdivided into a number of interconnected blocks, as illustrated in Figure 4, which allows the calculation to be parallelised over a cluster computer for improved computation time. This code has been used with success in the past for various expansion tube [6, 7] and shock tube [17] conditions, using both equilibrium and finite-rate chemistry gas-models.

Although the holding-time secondary diaphragm rupture model is expected to underestimate the thermochemical relaxation

through the unsteady expansion, it provides a simple pre-rupture flowfield that can be easily used as an initial condition for the `mbcns2` simulation. Using a holding-time of 10$\mu$s the stagnated test gas slug is calculated to be 4 mm long at rupture. A 4mm block thus precedes the acceleration tube, as shown in Figure 4, which is filled with the equilibrium stagnated test gas conditions. The upstream face of this block is a transient inflow boundary condition, applying the one-dimensional flow solution from the `L1d2` simulation uniformally over the inflow plane.

The single-temperature formulation of Park's $CO_2$–$N_2$ reaction scheme is implemented for the Navier–Stokes simulation. All the neutral dissociation and exchange reactions listed in Table 2 (reactions 1 to 16) are included in the Navier–Stokes simulations. A simplified analysis of the steady nozzle expansion is performed with the two-temperature gas model to assess the vibrational state of the final test gas. A quasi-one-dimensional space-marching approach is adopted using the standard conservation equations for steady flow with an area change.

#### Bluntbody shock layer simulation

The `poshax` (POst SHock relAXation) program is implemented to calculate the one-dimensional shock relaxation problem along the stagnation streamline of hypothetical bluntbody test articles. As the equilibrium post-shock temperature is expected to be approximately 7000 K, ionisation and radiation may be significant phenomena. The additional ionic reactions (reactions 17 through 27 in Table 2) are therefore included in the reaction scheme, and radiation is coupled to the flowfield. A spectrally resolved radiation model has been developed under the assumption of an optically-thin flowfield. The electronic populations of both molecules and atoms are assumed to be described by a Boltzmann distribution at the vibroelectronic temperature $T_{ve}$. Radiation is coupled to the flowfield solver through the radiative source term, $Q_{rad}$, and appears in both the total and vibroelectronic energy conservation equations.

| Radiator | Transitions | Source |
|---|---|---|
| CN | $B^2\Sigma^+ \rightarrow X^2\Sigma^+$ (Violet) | Jones [18] |
| | $A^2\Pi_i \rightarrow X^2\Sigma^+$ (Red) | Golden [19] |
| CO | $A^2\Pi \rightarrow X^1\Sigma^+$ (Fourth Positive) | Golden [19] |
| $C_2$ | $d^3\Pi_g \rightarrow a^3\Pi_u$ (Swan) | Golden [19] |
| C | 42 bound-bound transitions | Wiese [20] |
| O | 40 bound-bound transitions | Wiese [20] |

Table 3: Molecular band systems and atomic lines included in the spectrally resolved, optically thin radiation model.

The molecular band systems and atomic lines considered in the present analysis are summarised in Table 3. These transitions were identified by Park et al [10] as contributing the bulk of incident radiation to an aerocapture vehicle at 8 km/s. Atomic bound-free and free-free transitions are not considered in this analysis yet may be significant if substantial levels of ionisation are achieved.

#### Results and discussion

#### Lagrangian shock tube simulation

A driver slug length of 170 mm and piston velocity of 50 m/s at primary diaphragm rupture was determined through an idealised model of the free-piston compression. A driver slug temperature of 2800 K was selected through the matching of experimental conditions in a parametric analysis. A comparision of the `L1d2` and experimental static pressure history from shot x2s248 is shown in Figure 6. Although the experimental data shows a higher initial pressure rise for transducer ST1, excellent agreement is shown for the first 800 $\mu s$ of flow 0.5m downstream at ST3.

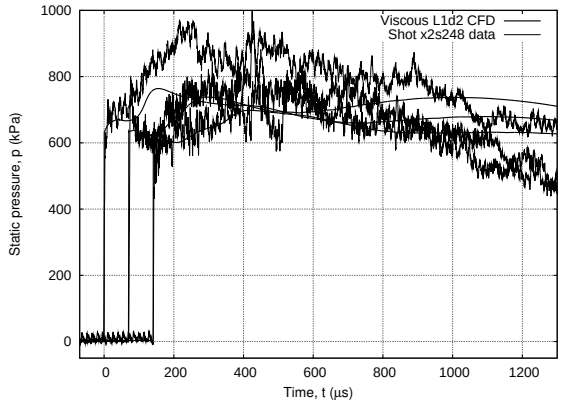


Figure 6: Comparision of static pressure traces from the viscous L1d2 CFD simulation with $T_{driver}$ = 2800K and shot x2s248 experimental data in the shock tube.

#### Secondary diaphragm rupture analysis

Equilibrium, nonequilibrium chemistry and nonequilibrium thermochemistry gas-models were implemented in the analysis of the secondary diaphragm rupture and subsequent unsteady expansion. For the inertial-diaphragm simulations, the contact surface was found to reach 95% of the assymptotic velocity 300 $\mu s$ after rupture. The species concentrations at this time were therefore taken to be representative of the fully expanded conditions.

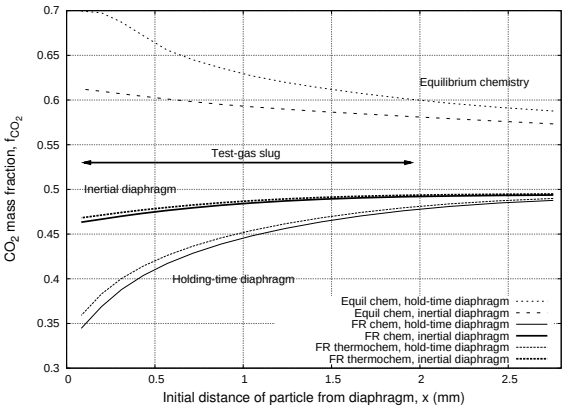


Figure 7: Fully expanded test gas $CO_2$ mass fractions following secondary diaphragm rupture ($t = t_{rupture} + 300\mu s$).

$CO_2$ mass fraction distributions at $t = t_{rupture} + 300\,\mu s$ for each of the Lagrangian simulations conducted are shown in Figure 10. $T_{ve}$ was found to equilibriate very quickly to $T_{tr}$, and there is little difference between the $CO_2$ mass fractions obtained from the nonequilibrium chemistry and thermochemistry simulations. The equilibrium gas-model simulations are seen to predict unrealistically high levels of recombination, as the chemistry is decoupled from the transient evolution of the unsteady-expansion. The equilibrium results have no physical relevance and will not be considered further.

Of considerable interest is the disparity shown between the inertial and holding-time diaphragm models. The holding-time model predicts lower levels of $CO_2$ recombination, with a much

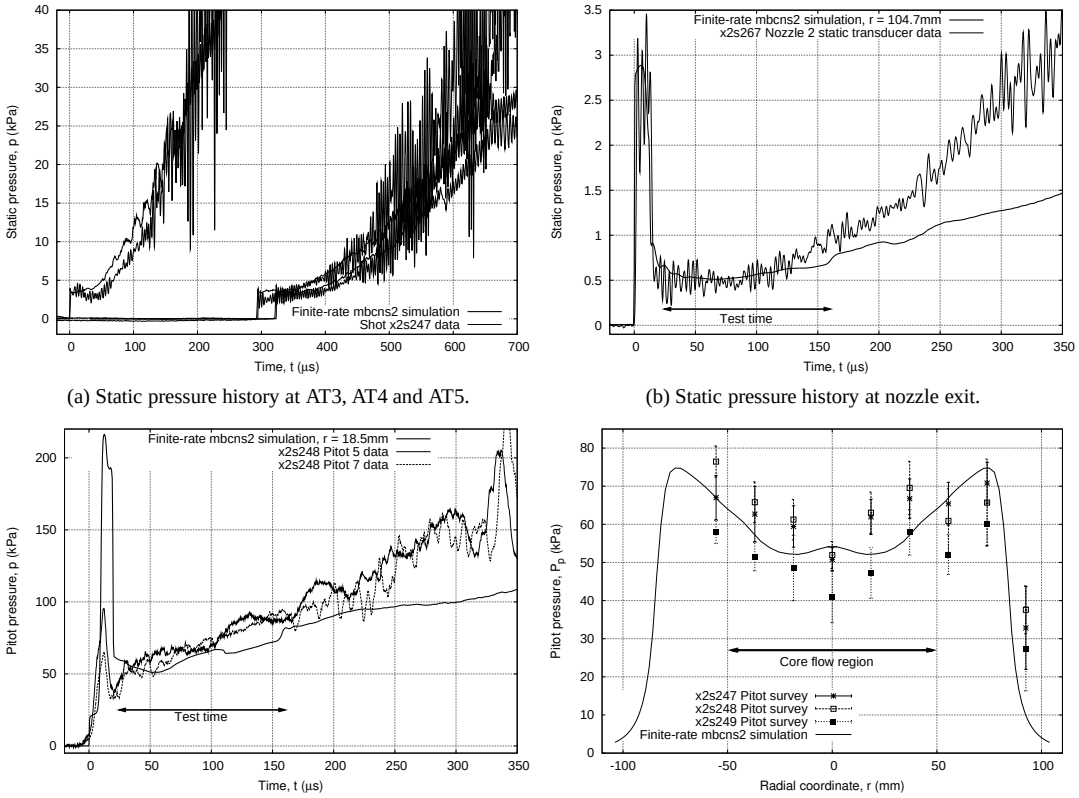


(a) Static pressure history at AT3, AT4 and AT5.

(b) Static pressure history at nozzle exit.

(c) Pitot pressure history 100mm downstream of nozzle exit.

(d) Pitot pressure profile 100mm downstream of nozzle exit at $t = t_{\text{rupture}} + 1175\mu s$.

Figure 8: Comparision of computational and experimental pressures through the acceleration tube and nozzle.

more pronounced variation over the slug when compared to the relatively uniform inertial-diaphragm results. This shows that the holding-time model predicts unrealistically large expansion rates for the test gas particles immediately upstream of the secondary diaphragm prior to rupture. The holding-time recombination levels begin to approach that of the inertial diaphragm simulations only at the very end of the test slug. From this analysis it can be seen implementing a holding-time rupture model for the condition at hand will result in $CO_2$ levels being underpredicted by between 25% and 4% over the test time.

### Navier-Stokes expansion tunnel simulation

Viscous Navier-Stokes simulations of the expansion tunnel flow were conducted with finite-rate chemistry and a pre-rupture flowfield described by the `L1d2` solution with a holding-time secondary diaphragm. Initial simulations with $37 \times 4500$ cells in the acceleration tube and a stagnated test gas slug length of 2mm resulted in unphysical pockets of hot, low density gas forming along the axisymmetric axis. Increasing the cell distribution to $43 \times 5155$ (1 mm squares, average) reduced this phenomena slightly, however disturbances were still observed during the test time. The test gas slug length was increased to 4 mm, corresponding to a hold-time of 10 $\mu s$, and the disturbances no longer formed during the test time. The stability of the flow during the test time for this final simulation is illustrated in the contours of pressure through the nozzle, Figure 9.

A comparision of the `mbcns2` solution with experimentally obtained pressure traces is shown in Figure 8. The freestream conditions from this simulations are shown in Table 1. The simulated secondary shock is seen to agree well with that from shot x2s247 which is close to the mean of the sample population. Excellent agreement with experiment is shown for both static and Pitot pressure at the nozzle exit for the first 200 $\mu s$ of flow. The simulated Pitot pressure profile 100 mm downstream of the nozzle exit shows reasonable agreement with that obtained through the experimental Pitot pressure survey. For the central 100mm of flow a test article is likely to occupy slight property variation exists, most noticeably at the extremities which has Pitot pressure 10% higher than at the central axis. Overall, the nonequilibrium `mbcns2` simulation shows sufficient correlation with experiment to justify use of the obtained freestream conditions for simulating the bluntbody shock layer.

### Nonequilibrium nozzle expansion analysis

The nozzle entrance conditions from the finite-rate `mbcns2` simulation were used as the initial conditions for thermal nonequilibrium, quasi-one-dimensional simulations of the steady nozzle expansion. The physical contour of the nozzle was used to calculate the flow area at each axial location, although in reality boundary layer development can result in the apparent area being considerably smaller. The temperature profiles shown in Figure 10 indicate the the transrotational and vibroelectronic modes have insufficient time to completely equilibriate during the expansion, although the nonequilibrium temperatures only differ from the equilibrium temperature by $\pm 1\%$. Such a small deviation from equilibrium is not anticipated to have significant influence on post-shock flow behaviour.

### Radiating shock layer analysis

The freestream conditions obtained from the finite-rate `mbcns2` simulation, as shown Table 1, are used for one-dimensional space-marching analysis's of the near post-shock region of radi-

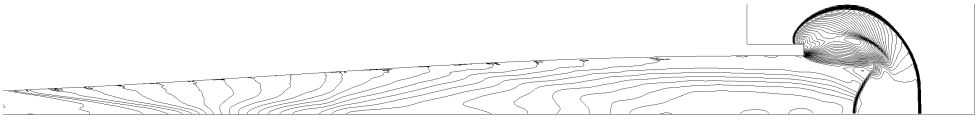

(a) $t = t_{\text{rupture}} + 1100\,\mu s$

(b) $t = t_{\text{rupture}} + 1150\,\mu s$

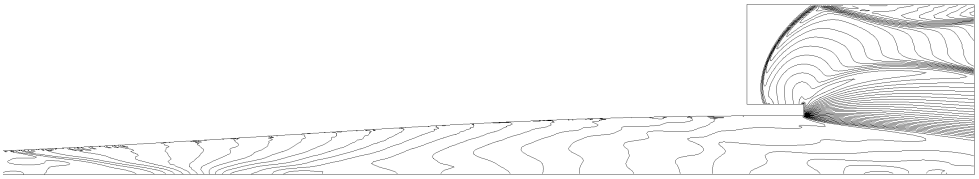

(c) $t = t_{\text{rupture}} + 1200\,\mu s$

Figure 9: Static pressure contours through the hypersonic nozzle during the first 100 $\mu s$ of test time.

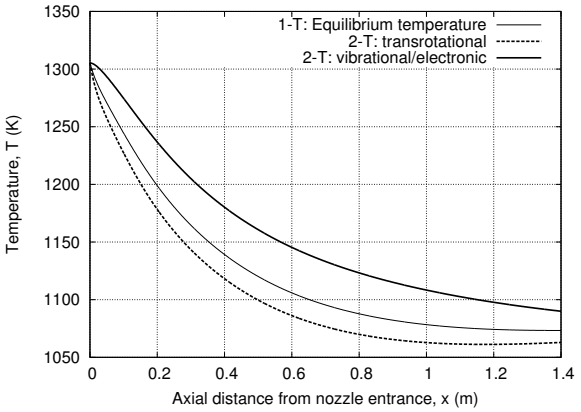


Figure 10: Test gas temperature evolution through the hypersonic nozzle for both single- and two-temperature gas-models.

ating shock layers formed over hypothetical test articles. Optically thin and radiatively coupled flowfields have been assumed for all simulations, and therefore the maximum possible radiative cooling effect is modelled.

The post-shock flow behaviour for hypothetical test models with various nose radii and corresponding flight conditions based on binary-scaling are compared in Figure 11. A flight length scale $L_{flight}$ of 1000 mm has been selected for all conditions — through matching of the binary-scaling parameter $\rho L$ between flight and experiment, the flight density for each nose radii is determined. An effective flight velocity ($v_\infty = \sqrt{2h_{total}}$) of 7030 m/s is used for all conditions. An ideal experiment is also defined to assess the influence of thermochemically excited freestream flow — this is a hypothetical binary-scaled condition where the freestream temperature, composition and velocity is identical to that encountered in flight. The trends in nondimensionalised distance to peak intensity $x_{peak}$ for various length scale ratios are illustrated in Figure 11a. The ideal experiment and flight conditions match up almost exactly, indicating radiation coupling has little influence on the initial excitation processes. $x_{peak}$ distances from the experiment conditions are consistently further than for the flight conditions, with the relative difference remaining constant for the full range of length scale ratios. The radiative heat flux $q_{rad}$ obtained from a tangent-slab analysis at the estimated wall location ($0.2L$) is shown in Figure 11b. The ideal and experiment condition trends are very similar over the majority of the length scale ratios considered, while the flight radiative heat flux levels are consistently lower. This indicates radiation-flowfield coupling is much stronger for the flight cases than in the subscale experiment — this is to be expected as the flight Goulard numbers are much higher due to the scaling up of density in the experiments. At length scale ratios below 1:50 experimental radiative heat flux levels are over twice the anticipated flight levels, while at length scale ratios above 1:10 flight levels are only overestimated by 20% or less. These results indicate that a thermochemically excited freestream and the disparity in radiation-flowfield coupling introduced by binary-scaling prevent similiarity with flight from being achieved.

#### Concluding remarks

A hybrid Lagrangian and Navier–Stokes simulation technique has been shown to perform adequately for a 25MJ/kg $CO_2$–$N_2$ expansion tunnel condition. The unsteady expansion of the test gas following secondary diaphragm rupture is, however, incorrectly described by a holding-time rupture model. Future simulations of this condition will implement an inertial diaphragm model to describe the pre-rupture flowfield for Navier–Stokes simulations of the acceleration tube, nozzle and dumptank flow. Slight thermal nonequilibrium is shown to develop through the steady nozzle expansion, with $T_{ve}$ and $T_{tr}$ deviating by up to $\pm 1\%$ from the equilibrium temperature $T$. As this deviation is much smaller than the simulated variation of $T$ over the test time, the assumption of thermal equilibrium is adequate. The obtained freestream conditions have been assessed for application to proposed bluntbody spectroscopy and subscale aeroshell experiments through a one-dimensional space-marching shock layer analysis. The chemically and vibrationally excited freestream test gas is found to prevent exact thermochemical similarity from being achieved, and the strong radiation–flowfield coupling predicted for the flight conditions cannot be reproduced experimentally. Irrespective of exact thermochemical similiarity with flight, expansion tunnel flows

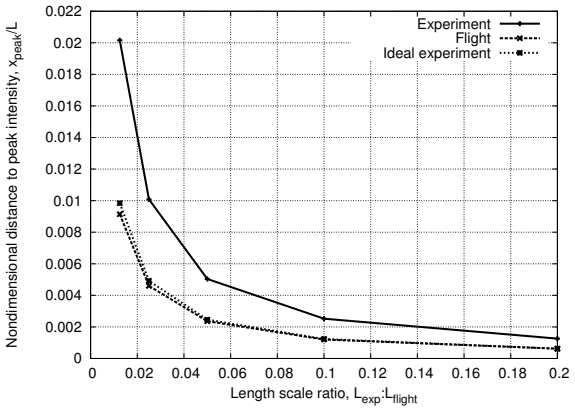


(a) Nondimensionalised distance to peak intensity $x_{peak}$.

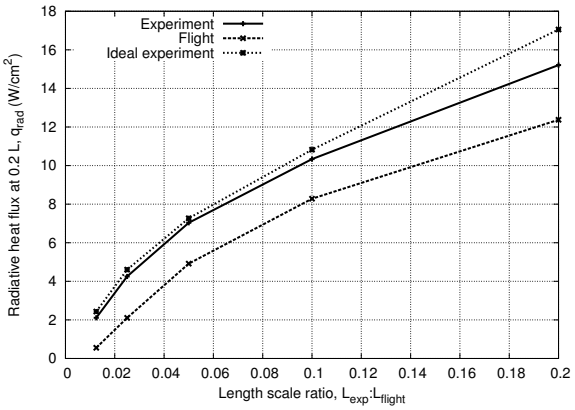


(b) Radiative heat flux $q_{rad}$ at $0.2L$.

Figure 11: Comparision of subscale and flight shock layer parameters for various length-scale ratios.

provide a valuable experimental reference for the coupling of chemical kinetic and radiation models to flowfield solvers. Further analysis needs to be conducted to determine the appropriateness of validating chemical kinetic models against binary-scaled conditions for application to true flight conditions.

#### References


[1] R.D. Braun, R.W. Powell, and L.C. Hartung. Effect of interplanetary trajectory options on a manned Mars aerobrake configuration. Technical Paper 3019, NASA Langley Research Center, 1 September 1990.

[2] C.S. Park, J.T. Howe, R.L. Jaffe, and G.V. Chandler. Chemical-kinetic problems of future NASA missions. *29th Aerospace Sciences Meeting, Reno, Nevada*, 7 January 1991.

[3] P. A. Gnoffo, K. J. Weilmuenster, D. R. Olynick, and H. Hamilton. Computational aerothermodynamic design issues for hypersonic vehicles. *Journal of Spacecraft and Rockets*, 36(1):21–43, 1999.

[4] D. Ellington. Binary scaling limits for hypersonic flight. *AIAA*, 5(9):1705–1706, 1967.

[5] B.R. Capra and R.G. Morgan. Radiative and total heat transfer measurements to a Titan explorer model. *14th AIAA/AHI Space Planes and Hypersonic Systems and Technologies Conference*, 2006.

[6] A.M. Brandis, R.J. Gollan, M.P. Scott, R.G. Morgan, P.A. Jacobs, and P.A. Gnoffo. Expansion tube operating conditions for studying nonequilibrium radiation relevant to Titan Aerocapture. *42nd Joint Propulsion Conference and Exhibit, 9 - 12 July 2006, Sacramento, California*, 2006.

[7] P.A. Jacobs, T.B. Silvester, R.G. Morgan, M.P. Scott, R.J. Gollan, and T.J. McIntyre. Superorbital expansion tube operation: estimates of flow conditions via numerical simulation. Paper presented to the 43rd AIAA Aerospace Sciences Meeting, Reno, NV, 10-13 January, 2005.

[8] M.P. Scott. *Development and modelling of expansion tubes*. PhD thesis, University of Queensland, 2006.

[9] I. Ndindabahizi, F. Mazoue, and L. Marraffa. Mars chemical kinetic models: a short review. In *European Space Agency, (Special Publication) ESA SP*, volume 629 SP, Rome, Italy, 2006.

[10] C.S. Park, J.T. Howe, R.L. Jaffe, and G.V. Candler. Review of chemical-kinetic problems of future NASA missions, II: Mars entries. *Journal of Thermophysics and Heat Transfer*, 8(1):9 – 22, 1994.

[11] S. Gordon and B.J. Mcbride. Computer program for calculation of complex chemical equilibrium compositions and applications. Part 1: Analysis. NASA Reference Publication 1311, United States, 1994.

[12] R.C. Millikan and D.R. White. Systematics of vibrational relaxation. *Journal of Chemical Physics*, 39(12):3209 – 3213, 1963.

[13] O. Knab, H.H. Fruhauf, and S. Jonas. Multiple temperature descriptions of reaction rate constants with regard to consistent chemical-vibrational coupling. *27th Thermophysics conference, July 6-8, 1992, Nashville, TN*, 1992.

[14] P.A. Jacobs. Shock Tube Modelling with L1d. Department of Mechanical Engineering Report 13/98, University of Queensland, November 1998.

[15] R.J. Bakos and R.G. Morgan. Chemical recombination in an expansion tube. *AIAA Journal*, 32(6):1316 – 1319, 1994.

[16] P.A. Jacobs. MB_CNS: a computer program for the simulation of transient, compressible flows. Department of Mechanical Engineering Report 7/98, The University of Queensland, St Lucia, QLD, 1998.

[17] R.J. Gollan, C.M. Jacobs, P.A. Jacobs, R.G. Morgan, T.J. McIntyre, M.N. Macrossan, D.R. Buttsworth, T.N. Eichmann, and D.F. Potter. A Simulation Technique for Radiating Shock Tube Flows. *26th International Symposium on Shock Waves (ISSW26)*, July 2007.

[18] J.J. Jones, R.E. Boughner, K.V. Haggard, J.E. Nealy, D.R. Schryer, and V.Z. Ernest. Radiative property data for venusian entry - A Compendium. Technical Report SP-348, Langley Research Center, 1974.

[19] S.A. Golden. Approximate spectral absorption coefficients of electronic transitions in diatomic molecules. *Journal of Quantitative Radiation Transfer*, 7:225–250, 1967.

[20] W.L. Wiese. *Atomic transition probabilities : a critical data compilation*. Washington : U.S. Dept. of Commerce, National Bureau of Standards, 1966.